APPLIED SCIENCES AND ENGINEERING

Scalable fabrication of Chip-integrated 3D-nanostructured electronic devices via DNA-programmable assembly

Aaron Michelson[1]†, Lior Shani[2]†, Jason S. Kahn[1], Daniel C. Redeker[3], Won-Il Lee[4], Katerina R. DeOlivares[3], Kim Kisslinger[1], Nikhil Tiwale[1], Hanfei Yan[5], Ajith Pattammattel[5], Chang-Yong Nam[1,4], Vlad S. Pribiag[2]*, Oleg Gang[1,3,6,7]*

DNA-based self-assembly methods have demonstrated powerful and unique capabilities to encode nanomaterial structures through the prescribed placement of inorganic and biological nanocomponents. However, the challenge of selectively growing DNA superlattices on specific locations of surfaces and their integration with conventional nanofabrication has hindered the fabrication of three-dimensional (3D) DNA-assembled functional devices. Here, we present a scalable nanofabrication technique that combines bottom-up and top-down approaches for selective growth of 3D DNA superlattices on gold microarrays. This approach allows for the fabrication of self-assembled 3D-nanostructured electronic devices. DNA strands are bound onto the gold arrays, which anchor DNA origami frames and promote ordered framework growth on the specific areas of the surface, enabling control of the lateral placement and orientation of superlattices. DNA frameworks selectively grown on the pads are subsequently templated to nanoscale silica and tin oxide (SnO_x) that follow the architecture, as confirmed by structural and chemical characterizations. The fabricated SnO_x superlattices are integrated into devices that demonstrate photocurrent response.

INTRODUCTION

The generation of functional devices using top-down fabrication has been the foundation of modern technology. However, the limitations of top-down methods for features with sub-50 nm hinders the realization of advanced concepts based on three-dimensional (3D) architectures for electronic devices, quantum information systems, optical metamaterials, and neuromorphic computing (*1*–*4*). The desire to gain 3D structural control and exploit nanoscale phenomena has encouraged the development of bottom-up nanotechnology methods that can use molecular forces to prescribe nanoscale interactions and material assembly for building systems with desired functions. Bioinspired bottom-up material fabrication approaches to exert control on the nanoscale leverage the structural diversity and interaction specificity of DNA to build nanomaterial from colloids and nanoparticles (*5*–*8*). Self-assembly driven by DNA-programmable interactions is an approach that allows for both structural control and prescribed material placement at the nanoscale, yielding emergent metamaterial properties (*9*–*12*). DNA nanotechnology is anticipated to enable a broad range of biochemical and semiconductor technologies (*13*). The bottom-up approaches for controlling the organization and placement of functional components could be integrated with conventional lithography-based fabrication for establishing a 3D nanomanufacturing paradigm.

Prior attempts to integrate DNA with typical top-down lithography for device application have focused on using DNA either for a template (*14*, *15*) or for its bio-recognition capacity to capture a signal from a liquid analyte (*16*, *17*). Further integration can open a range of functional material applications, leveraging DNA's capability to direct the formation of 3D-organized nanomaterials (*7*, *18*), particularly, using DNA origami frameworks (*12*, *19*). The ability to not only self-assemble the crystalline nanostructures but also to place them at the desired location is a key technological capability needed for the realization of 3D devices, which is currently lacking. The prospect of creating functional devices from these resulting superlattices arises from their ability to incorporate functional payloads, such as nanoparticles, quantum dots, enzymes, proteins, and others, into the framework (*12*) and to provide scaffolding for building inorganic framework architectures (*20*).

Achieving macroscale control over self-assembled DNA-based frameworks presents a challenge in prescribing the placement and orientation of the framework crystals on a substrate (*21*). This is crucial in device fabrication, where precise positioning is required to create functional devices, and for their scalable manufacturing. This issue arises because the lattices are typically grown in a solution and only subsequently drop-cast onto a substrate (*12*, *19*). This approach is ill-suited for integrating these self-assembled structures into devices. Lattice can be processed using a focused ion beam (FIB) to translate the sample to electrical contacts for further investigation (*22*) or etched after the physical deposition of the thin metallic film (*23*), but these are all extremely low-throughput approaches that typically enable only a couple of devices to be created and tested.

Conversion of individual DNA architectures and their assemblies into silica form makes it possible to preserve DNA structures

[1]Center for Functional Nanomaterials, Brookhaven National Laboratory, Upton, NY 11973, USA. [2]School of Physics and Astronomy, University of Minnesota, Minneapolis, MN 55455, USA. [3]Department of Chemical Engineering and Department of Applied Physics and Applied Mathematics, Columbia University, New York, NY 10027, USA. [4]Department of Materials Science and Chemical Engineering, Stony Brook University, Stony Brook, NY 11794, USA. [5]National Synchrotron Light Source II, Brookhaven National Laboratory, Upton, NY 11973, USA. [6]Center for Nanomedicine, Institute for Basic Science (IBS), Seoul 03722 Republic of Korea. [7]Department of Nano Biomedical Engineering (NanoBME), Advanced Science Institute, Yonsei University, Seoul 03722 Republic of Korea.
*Corresponding author. Email: vpribiag@umn.edu (V.S.P.); og2226@columbia.edu (O.G.)
†These authors contributed equally to this work.

over a broad range of environmental conditions (*24*, *25*). Metamaterials made using this strategy have demonstrated applications in high-strength, lightweight materials and enabled explorations of quantum effects in a 3D nano-matrix after coating with superconducting materials (*22*, *26*). Along with the successful conversion of DNA structures into silicon carbide (*27*), calcium phosphate (*28*), and silica-silver (*29*) materials, the recently demonstrated 3D templating strategy allows for the creation of 3D replicas of DNA frameworks in the form of insulators, conductors, and semiconductors (*20*). The range of possible properties and functions makes this a desirable nanofabrication platform; however, several challenges remain. The DNA structures are generally formed in solution, far from the intended surfaces. Crystals deposited from drop-casting this solution often aggregate uncontrollably with a random orientation at surfaces. The bulk self-assembly lacks the capability to direct assembly where desired, and thus, it substantially limits the application of assembled structure, which might require well-ordered and well-oriented organizations of crystals over the large areas.

In this work, we established the large-scale integration of 3D DNA-programmable assembly and inorganic templating with a traditional, scalable nanofabrication workflow for creating electronically functional devices. We selectively grow 3D DNA frameworks at specific prescribed locations on a silicon wafer across a millimeter-wide area, functionalize them volumetrically with semiconducting material, and characterize the formed DNA-assembled devices. This method demonstrates the capability to direct self-assembly of anisotropic nanoscale components (DNA origami frames) with directional interactions at the defined surface area. The directional interactions of the frames promote a particular frame's orientation at the surface and give rise to the stabilization and growth of the specific crystallographic planes of the assembled lattice. Moreover, since the DNA frame assembly approach permits both the incorporation of different types of nano-cargo (*12*) and DNA inorganic templating (*20*), the pattering and surface growth further provide a pathway for device fabrication.

First, we developed a method for selective growth of self-assembled DNA superlattices on an array of gold square-shaped patterns on a silicon substrate using site-specific attachment via thiol-modified single-stranded DNA (ssDNA) on the gold. The DNA framework lattice was then transitioned to the solid state via sol-gel synthesis of silica (*25*) and templated with uniform, conformal incorporation of tin oxide (SnO_x) semiconductor via vapor-phase infiltration (VPI). The structural and chemical composition of the formed structures were confirmed by scanning electron microscopy (SEM), cross-sectioned with FIB, and examined via scanning hard-x-ray tomography (*30*). By prescribing patterns of growth of the SnO_x lattice frameworks on silicon wafers, followed by electrode attachment to a 3D SnO_x framework domain, we demonstrate the fabrication of a 3D-nanostructured electronic device based on the self-assembled superlattices. We further probed the current-voltage (*I*-*V*) characteristics of a device consisting of three SnO_x superlattices connected in series and revealed its photocurrent response.

RESULTS

To establish a large-scale patterning for the assembly of functional materials, a scalable synthesis approach is required to span the macroscale area. To address this challenge, we considered selective area growth techniques that have proven to be useful in growing nano- and microscale structures such as metals (*31*), III-V (*32*), and IV-VI (*33*) compound semiconductors. In the case of semiconducting materials, the substrate for epitaxial growth is coated with a hard mask, which consists of nanoscale geometries that facilitate growth in the exposed substrate and inhibit growth on undesired regions. This approach makes subsequent steps of fabrication simpler since the nanostructures are placed deterministically on the growth substrate, thus increasing the yield of fabricating functional devices. We apply similar principles to DNA-based materials by planting thiolated ssDNA anchors on a gold-patterned surface, which allows directing the growth of 3D self-assembled DNA-based materials at predefined locations. Similar approaches have been demonstrated on nanoparticle-based nanolattices, leveraging gold surfaces with ssDNA anchors to attach and orient nanocrystals (*34*, *35*), as well as with individual 3D DNA origami (*36*, *37*). In contrast to assembly of isotopically interacting nanoparticles, DNA origami frames have a "valence" of interactions (*12*, *38*), which can influence the orientation of frames at the surface and a growth of self-assembled origami crystals. We hypothesize that these directional interactions can stabilize and orient surface-assembled crystal morphologies due to the preferential formation of specific planes. From application point of view, DNA origami frames are capable of carrying of diverse functional nano-cargo and have the ability to integrate lattices formed by frames with surfaces, which allow for creating different types of organized 3D nanomaterials in a device-suitable geometry.

Here, we demonstrate that the integration of DNA framework assembly with surface patterning, followed by inorganic templating and lithography, provides a full-cycle methodology for creating functional 3D-nanostructured electronic devices. Superlattices of DNA octahedral frames with an edge length of ~29 nm are formed via inter-vertex DNA-prescribed interactions (*25*, *26*, *39*). Subsequent superlattice growth requires a set composed of two DNA origamis: one having binding strands X with eight encoded bases for recognition on its vertices and the other having the binding complement X′. Each octahedron thus coordinates with six neighboring octahedra to yield a simple cubic superlattice, adopting a cubic Wulff structure when unimpeded in solution.

We depict the DNA framework growth on a patterned surface with ssDNA-encoded anchoring sites in Fig. 1. First, to incorporate selective growth, we lithographically patterned arrays of gold squares on silicon with native oxide. The typical pattern area covered between 1 and 10 mm, with patches from 15 nm by 15 μm down to 150 nm by 150 nm with gap spacings from 10 μm down to 100 nm, respectively. Next, once the gold has been cleaned via oxygen plasma, thiol-modified DNA is attached to the surface (see table S1 and fig. S1 to S5) (*35*). The surface attachment strands (X and X′) have a thiol functional group on the 5′ end of the ssDNA strand, a 15-base poly-thymine spacer, and an 8-base complementary sequence to vertex sequence overhangs on the octahedron origami (table S1). After washing the surface from strands excess, DNA frames and the surface were sealed together and subjected to thermal annealing to allow for the frames to assemble into superlattices on the surface, as schematically shown in Fig. 1A. Control experiments demonstrate that without a specific bond at the surface, crystals grow with a random orientation with respect to the surface, tending to fall on [100] type facets. In addition, we did not observe a statistically significant difference to the size of obtained crystals when annealing in a polymerase chain reaction (PCR) tube or flat cell; see fig. S1.

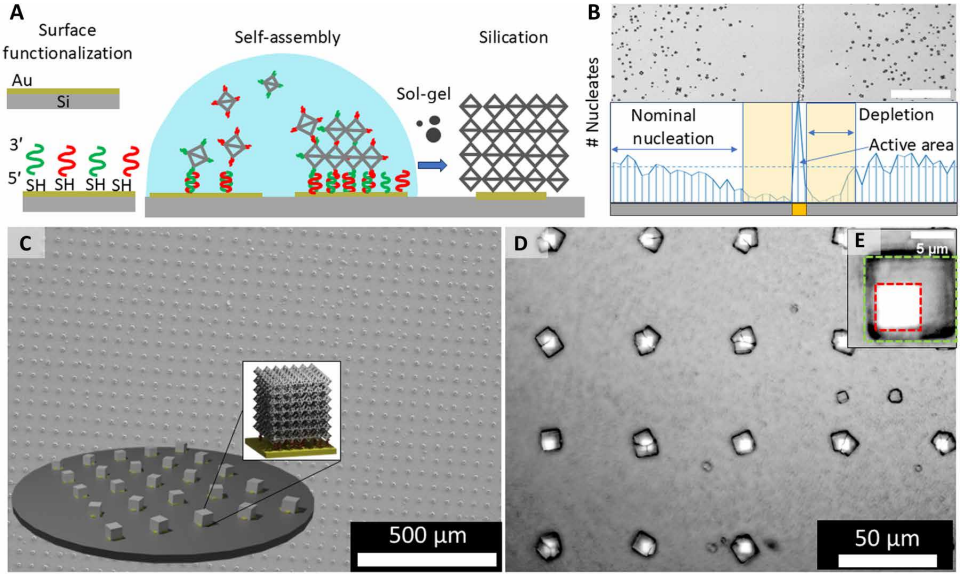

Fig. 1. Area-selective growth of DNA superlattices on surfaces. (**A**) Schematic of selective area growth of DNA superlattices on gold pads (yellow) functionalized with DNA strands (green and red). A gold-patterned silicon substrate immobilizes DNA strands with encoded complementary interactions using gold-thiol chemistry, followed by hybridization of target origami frames to the specific areas of the surface and lattice assembly. Sol-gel synthesis across a patterned silicon substrate area is used for silica templating of formed frameworks. (**B**) Top, optical microscope image of epitaxial growth of superlattice from a DNA functionalized gold line. Bottom, frequency plot of nucleates from the above image counting the number of crystals in each column. Annotated on the plot are two windows 60 μm wide corresponding to the depletion region. Scale bar, 50 μm. (**C**) Low-magnification DNA superlattice crystals grown across a 10 mm–by–10 mm pattern of gold pads. Scale bar, 500 μm. (**D**) Optical microscope image of the array of 5 μm–by–5 μm gold patches on silicon with self-assembled DNA superlattice templated to silica, composed of singular and polycrystalline domains. (**E**) Magnified view of nanolattice (within green dotted region) grown on a pad (red dotted region).

Control of the crystal growth at the surface can be likened to island epitaxy, which predicts a characteristic length scale for epitaxial growth (*40*, *41*). To derive the distance required for placing pads apart from each other to achieve this condition, we empirically evaluated the nucleation away from the functionalized gold strip, which is approximately 10 μm wide (Fig. 1B and fig S3). Analysis of optical microscopy using Segment Anything and Fast Segment Anything software (fig. S4) (*42*, *43*) shows that nucleation is found to deplete within 60 μm. For a design with gold pads approximately 50 μm apart, we can reduce spurious nucleation between patches, as shown in Fig. 1C and figs. S2 and S5 to S6. Patch sizes from 1 to 5 μm resulted in the more prominent formation of singular crystals at the surface, whereas for patches with sizes above 5-μm crystals with multiple domains were observed (figs. S6 and S7). For the octahedral motif, this is expected, given a correlation length of 1 to 2 μm for bulk-grown crystals at similar conditions, as measured by small-angle x-ray scattering (*26*). However, it is possible to potentially further constrain growth by lowering the concentration or introducing a specialized annealing pathway. From SEM of a 40-by-40 array with 1600 5-μm pads after the initial synthesis, up to 97% were occupied, among which more 80% were occupied by single crystals (some with defects); see Fig. 1D and figs. S7 and S8. These domains nucleate from the patch and grow over the region until they deplete the monomer from the solution. Figure 1E shows a crystal with a gold patch visible through the crystal, which indicates that the self-assembly process results in the crystal overgrowth over the patch area. This feature is useful for device fabrication since overgrowth allows for contacting the assembled structure without shorting current through the underlying gold pad. Additional growth of the DNA crystal can be accomplished by introducing further monomers to the chamber (fig. S5B), which can be potentially used for the formation of contiguous lattices across the pattern.

We next explore affecting a preferential orientation of crystal grown from the surface through DNA frame bindings with surface-grafted ssDNA. This can be achieved by the selection of DNA type grafted to the surface. In this case, with a set of two complementary origami, the inclusion of only one binding strand on the surface (either X or X′) leads to the assembly of crystals oriented along the (111) direction; see Fig. 2A and figs. S9 to S13. The crystals truncate in the (111) direction out of the plane and proceed to grow along minimum energy pathways leading to pyramidal Winterbottom Wulff morphology, shown in Fig. 2A at 52°. If strands X and X′ are attached to the surface, crystal growth preferentially occurs along the [100] directions (*Z* orientation), while there is no constraint in the *XY* plane (Fig. 2B and fig. S14).

To further investigate the surface interaction with the assembly, we cross-sectioned the sample by FIB/SEM and viewed inspected regions grown in the (111) and (100) orientations, shown in Fig. 2 (A and B). The region of the crystal growth closest to the surface exhibits more disorder compared to regions further from the interface. This is likely due to some degree of heterogeneity of attachment of thiolated ssDNA strands to the gold pads and constraints for rearrangements during annealing near the surface (figs. S11 to S14). Hard x-ray tomography of surface-grown superlattice allows us to evaluate volumetrically the structure and defects of these lattices. Shown in Fig. 2D is a 3D reconstruction (*44*, *45*) cross-sectional view into the interior of a nanolattice, which shows domains and voids grown from a gold surface. K-space investigation of the sample shows domains cluster along the (001) planes matching macroscopic observations of preferential alignment of crystals as seen

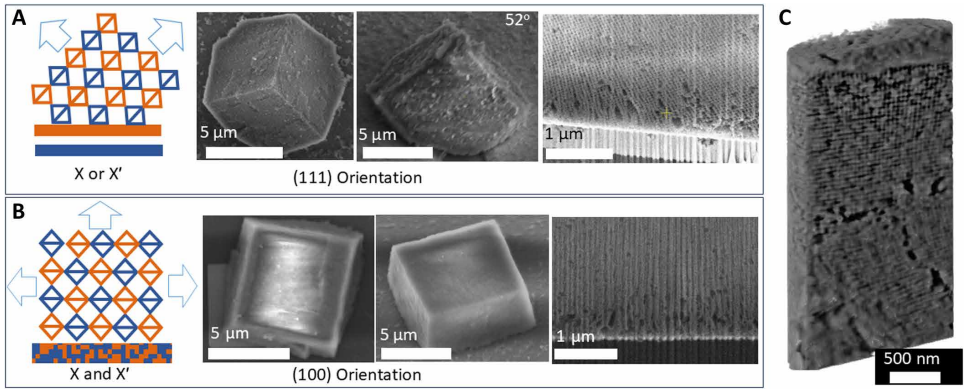

Fig. 2. Orientated growth of superlattices and interfacial defects. (**A**) Monofunctionalized surfaces with X or X′ strands lead to superlattice oriented in the [111] direction as complimentary origami assembly along {100} directions from an initial (111) plane. From left to right, SEM images, top-down and 52°, followed by a cross-sectional view of a nanolattice, which displays voids and coalescence of origami arrays. (**B**) Bifunctionalization of the surface with both X and X′ strands, leading to [100] oriented domains. From left to right, SEM images, top-down and a 45°, followed by a cross-sectional view of nanolattice voids and defects within the first 1 µm from the interface. (**C**) Hard x-ray tomography of a surface-grown superlattice, cross-sectional view of the nanostructure from a (100) oriented grain. Multiple domains are visible within the superlattice as evidenced by discontinuities in the lattice geometry often accompanied by voids to accommodate lattice mismatch.

from optical and electron microscope in the *Z* direction. 3D visualization indicates 2° to 7° of misalignment between the domains with respect to the surface and coalesces into a single domain as the crystal grows up in the *Z* direction. Domains accommodate each other through vacancies and pores that allow misorientations of crystal grains within the superlattice (figs. S15 and S16) due to the flexibility of interframe bonds (*30*). We extrapolate that misorientations and strain in the lattice are resolved within 1 µm from the surface, as corroborated by cross-sectional views into other crystals.

To fabricate devices based on the 3D DNA frameworks, the surface-grown nanolattices were converted to silica via A-gel synthesis following a protocol (*25*) modified for our application. After silication, nanolattices—specifically, individual nanoscale struts within the nanolattices—were infiltrated with tin oxide via micro-dose VPI (*46*, *47*), an ex-situ organic-inorganic hybridization technique derived from atomic layer deposition (ALD), which has demonstrated the ability to incorporate semiconducting metal oxides into a DNA-structured template (*20*), thus allowing us to engineer the nanolattice to be light-sensitive. After the metal oxide infiltration, the array was thermally annealed at 600°C for 5 min in O_2 within a rapid thermal processor (RTP). This was followed by gold contact deposition (see Fig. 3A for a schematic representation).

Figure 3B shows an SEM image of nanolattice device "D1," at a perspective angle after being contacted with gold (Au) electrodes. The electrodes are about 120 nm thick and conform to the natural surface shape of the nanolattice domain. The presence of Sn was confirmed by energy-dispersive spectroscopy (EDS) measurement of the nanolattice. An EDS map of the nanolattice after electrode deposition (Fig. 3C, a top-down perspective) shows the targeted Sn content within the nanolattice with minimal ancillary deposition (<1 wt %; figs. S10 and S11) on the surrounding silicon/SiO_2 substrate (see also figs. S17 and S18). High-resolution SEM (Fig. 3D) of the surface structure shows a coating of material with clear voids in the space between octahedral units. Subsequent scanning transmission microscopy (STEM) of a cross section from the infiltrated SnO_x superlattice confirms the 3D conformal coating of SnO_x on the interior silica surface of the nanolattice; see Fig. 3 (E and F) and fig. S19. The EDS spectra from the center of a crystal on a gold pad, shown in Fig. 3G, displays spectra of tin, silicon, and gold (from the underlying pad). The associated atomic percent of the tin in the sample is estimated to be 9 atomic % (at %) of the nanolattice compared to 38.6 at % silicon (see fig. S18). X-ray diffraction (XRD) characterization of the annealed RTP lattice array (Fig. 3H) is consistent with signatures of cassiterite (SnO_2) with broad peaks indicating nanocrystallites and two gold peaks associated with the gold pads and markers near the superlattice structures. The peak fitting of the tin oxide first peak from the XRD suggests SnO_2 crystal sizes of the order of 2 nm (fig. S20).

We then investigated the behavior of tin oxide superlattices under bias and photocurrent response by measuring three SnO_x superlattices individually and connected in series, as shown in Fig. 4A. The connections diagram between the three SnO_x superlattice devices is seen in the colored overlays in Fig. 4A. Figure 4B and figs. S21 and S22 show the measured current as a function of the applied voltage (*I-V* curves) across a single SnO_x superlattice device (curve D1), a series connection of two devices (curve "D1+D2"), and of three devices (curve "D1+D2+D3"). The *I-V* curves show asymmetry between negative and positive voltage bias. At negative voltage bias, the measured current is substantially lower compared to that obtained for positive voltages of the same magnitude, which is most likely caused by a difference in the contact resistance between electrodes of each superlattice.

The differences in transport between crystals is likely due to a mix of extrinsic effects associated with electrical contacts and crystal morphology and intrinsic factors, such as grain boundaries and chemical compositional changes throughout the crystals; both effects can contribute to the observed response behavior. Overall, the transport behavior of the SnO_x-superlattice is described by a Poole-Frenkel emission (PF) model (fig. S23) (*48*). In PF emission, an electric field of sufficient strength facilitates the thermally assisted excitation of carriers from localized states (for example, due to atomic-scale defects such as vacancies) to the conduction band. PF transport is caused because of processes occurring in the bulk of the material rather than at the contacts. The PF emission model has

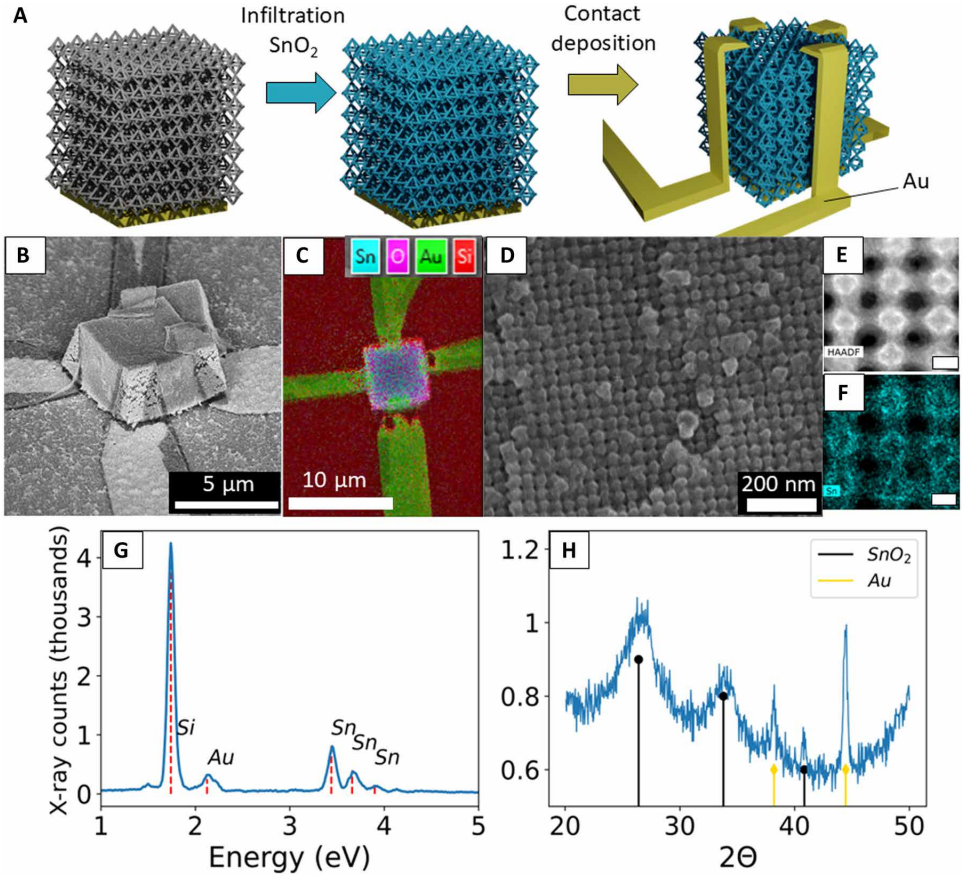

Fig. 3. Fabrication of the device based on 3D Sn-framework. (**A**) Schematic of the preparation of SnO_x-SiO_2 superlattices using VPI followed by thermal annealing and electrode deposition. (**B**) SEM of the fabricated device with electrodes on four corners. (**C**) SEM-EDS map of selective area–grown superlattice coated with tin and contacted with gold electrodes. (**D**) High magnification SEM of the lattice, top surface. (**E**) STEM high-angle annular dark field (HAADF) image of cross-sectioned nanolattice. Scale bar, 20 nm (**F**) STEM-EDS map from location E, which displays the tin-coated superlattice, with the thickness of the tin estimated between 2 and 4 nm; see also STEM HAADF and EDS maps in fig. S19. Scale bar, 20 nm. (**G**) EDS spectroscopy of tin oxide nanolattice and gold patch beneath the structure. (**H**) Grazing incidence XRD of SnO-SiO_2 superlattice array that shows broad SnO_2 peaks corresponding to the thin nanostructure on the superlattice along with sharp gold peaks from the ~60-nm–thick gold surface patches.

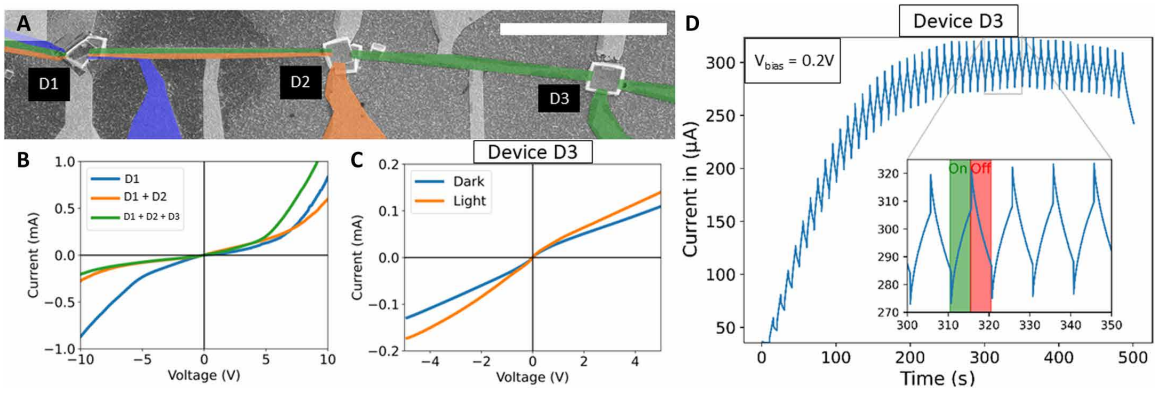

Fig. 4. Photocurrent response of devices with integrated 3D SnO_x superlattices. (**A**) SEM image of the lattices measured with false color added for the current pathway. Scale bar, 30 μm. (**B**) Current-voltage curves for superlattices tested individually and connected in series. (**C**) Current-voltage curve measured on nanolattice device three D3 in dark (blue) and under UV light (340 nm) illumination (orange). Scale bar, 10 μm. (**D**) Current versus time measurement at constant voltage bias (0.2 V) as light exposure was turned on/off every 5 s on D3. The initial drift in the measured current saturates at around 300 μA. The inset shows a zoom-in region of steady-state behavior with a 50-μA response.

been previously used to explain the transport behavior of disordered semiconductors (*49*). This argument is supported by our STEM and SEM characterizations that demonstrate a network of nanocrystalline domains with grain boundaries (i.e., atomic defects) of superlattices, similar to those of a disordered material.

The photocurrent response of our metal oxide nanolattice when exposed to light can be attributed to the increased charge carrier density from the excitation across the semiconductor bandgap and oxygen desorbed from the surface and grain boundaries, which can release localized electron charge carriers and lower the barrier height for inter-grain charge transport (*50*). As shown in Fig. 4C, a single superlattice domain has a repeatable steady-state *I-V* response that is more conductive when exposed to ultraviolet (UV) light (340 nm). When the light is turned off, the superlattice returns to its initial, more resistive, state. To investigate the temporal behavior of the photocurrent, we tracked the Sn-superlattice at a constant bias voltage of 0.2 V; see Fig. 4D. The superlattice was cycled every 5 s with UV illumination. An initial increase in the device conductivity (sensor-drift) at the beginning of this cycling process was observed, which is likely due to the gradual population filling of the electronic defect states by photoexcited charge carriers and their slow depopulation from the states once trapped. Once these defect states were completely filled by the photoexcited carriers, the device current then reached a steady-state operation around 300 μA with a light response/recovery of 50 μA as shown in Fig. 4D. Further improvement of the device performance would be expected after thermal annealing optimization of the superlattice (*50*, *51*).

DISCUSSION

In summary, we demonstrated a method for large-area selective growth of 3D self-assembled DNA superlattices and their subsequent templating with a semiconducting material, followed by device integration. This study demonstrates a proof of principle on creating a 3D-nanostructured device by means of DNA-programmable self-assembly on silicon substrates. Given the ability to form complexly ordered DNA organizations (*12*, *38*, *52*, *53*) and the inclusion of nanomaterials either via nanoparticle placement in a 3D DNA scaffold or inorganic templating of scaffolds (*20*), the developed strategy permits the fabrication of 3D devices over large areas. Moreover, since the patterning approach is not limited to silicon surfaces, such devices can be built on different types of surfaces. To transform the developed approach into device fabrication technology, it is required to address several key points, as revealed by this study. Specifically, we observed several sources of defects when lattices assembled on patterned surfaces, such as some degree of lattice defectivity in the first several layers at the solid interface and assembly of lattices as domains rather than single crystals within individual pads. Besides, atomic-level imperfection of functional inorganic coating (SnO_x) of nanoscale features can affect the device performance, and, since our devices are porous, this can be further improved through careful optimization of thermal and etching procedures. In this respect, our study explored the major critical parameters influencing the morphology and fidelity of formed DNA crystals on patterned surfaces, including pattern design, surface functionalization with DNA, and conditions for lattice formation. On the side of device fabrication, while we demonstrate an ability to control crystal morphology, further development of methods for orientating lattices in the *XY* plane will be beneficial for simplifying the scaling of device manufacturing. Overall, the large surface-to-volume ratio of the SnO_x superlattices, high parallel synthesis capability of many crystals, and precise, high-fidelity substrate positioning open the door to incorporating self-assembled DNA nanostructures as material templates into a wide range of devices, such as gas sensors (*54*), supercapacitors (*55*), and photonic crystals (*53*). The demonstrated approach opens a path for using DNA self-assembly as a nanofabrication technique.

MATERIALS AND METHODS

Experimental design

Herein is described experimental methods and materials needed to create DNA origami nano-objects that can self-assemble to predefined gold pads when combined in solution to form ordered nanolattices. This is followed by templating the soft-matter to a solid-state inorganic nanolattice for subsequent functional metal oxide and contact deposition.

DNA origami synthesis

DNA origami octahedron were formed following literature (*26*). We mix M13mp18 DNA scaffold and DNA staple strands at a 1:5 ratio in tris buffer (40 mM tris acetate) with 12.5 mM Mg^{2+}. Origami was then folded into an octahedron through slow cooling in a PCR from 90°C to room temperature over 20 hours.

Surface functionalization

Silicon with gold pads (fabrication detailed below) were cleaned with O_2 plasma, 10 min, 100 mW power, reactive ion etching. To prepare the thiolated ssDNA for attachment to the surface, 4 μl of 800 μM strand X and 4 μl of 800 μM strand X′ were combined with 16 μl of 0.5 M tris(2-carboxyethyl)phosphine in a 0.2-ml tube for 30 min in a shaker. To this, 200 μl of 10 mM phosphate buffer with 1 M NaCl was added. Then, the solution was encased to the surface with the aid of a gene frame (25 or 65 μl) overnight or over the weekend, depending on the desired coverage. After the designated amount of time, the seal was broken on the gene frame, and the surface was washed with copious amounts of water. At this point, the surface was either used immediately or kept in buffer and wet.

Surface assembly

If the chips are small, the assembly can take place in a conventional 96-well plate PCR. To allow for a larger surface area, the large piece can be annealed using a conventional PCR using a flat adapter plate. While the surface is still wet, a premixed tube with origami A and origami B is aliquoted onto the surface and sealed in a gene frame. Annealing is then performed on a flat PCR adapter plate with the top lid held at 40°C with the bottom thermocycler ramping to 50°C for 10 min, followed by slow cooling from 48°C toward room temperature at a ramp of −0.2°C/hour or until at least 45°C.

Silication

To transform the soft matter to a solid state, subsequent silication was performed following lattice annealing. Gentle washing of the samples was performed in a 50-ml tube or flask, with enough agitation just to remove excess nanolattice. A 1.5-ml tube should be prepared with 445 μl of Deionized Water (DI) water, with 10×

TE + Mg buffer (400 mM tris and 100 mM magnesium acetate), 1 μl of 3-aminopropyltriethoxysilane, and 3.5 μl of tetraethyl orthosilicate (TEOS). This is suitable for small chips in 0.2-ml tubes. For larger pieces, the recipe was scaled up at least 30× for use in a 50-ml tube. The samples were shaken 1 to 4 hours before washing with water and blow dried with dry air. The samples were then baked on a hot plate set to >100°C to further remove water. If it is not possible to load the sample into a 50-ml tube or smaller, the precursor were loaded into a gas tight sealing system overnight and placed on a thermomixer at 400 rpm. The samples were inspected under an optical microscope to ensure complete silica coating before quenching the reaction in water and drying in air or on a hot plate.

Gold surface pad preparation

A bilayer resist consisting of two layers of poly(methyl methacrylate) 495 K PMMA A4 and a top layer of 950 K PMMA A2 was spin-coated on a Si wafer (4000 RPM, 5-min bake at 180°C). Square patterns were created using conventional e-beam lithography. The pattern is developed in 3:1 IPA (Isopropyl alcohol):MIBK (methyl isobutyl ketone) for 80 s followed by 60 s IPA rinsing. After developing the exposed area, a layer of 10 nm of Ti (1 Å/s) and 60 nm of Au (2 Å/s) was deposited using an e-beam evaporator (CHA) followed by lift off in warm (50°C) acetone.

SnO_x infiltration

The infiltration of SnO_x into the silicate superlattices was carried out in a commercial ALD system (Cambridge Nanotech, Savannah S100) at 85°C using tetrakis(dimethylamido)tin (TDMASn) as metal-organic precursors along with water as an oxidant. The micro-dose infiltration of SnO_x was performed 10 cycles with the TDMASn and water precursor exposure period of 600 s; the precursor pulsing was repeated every 60 s during each exposure period (total of 10 repeated pulses for 600 s by pulsing TDMASn for 0.2 s and water for 0.04 s). A single SnO_x infiltration cycle by the micro-dose protocol consists of, in sequence: TDMASn exposure for 600 s under a static vacuum (~0.3 Torr), purging the chamber for 600 s using N_2 [100 standard cubic centimeter per minute (SCCM)], the water vapor exposure for 600 s under a static vacuum (~0.3 Torr), and chamber purging using N_2 (100 SCCM) for 600 s. The infiltration was followed by the initial removal of the organic polymer matrix by oxygen plasma ashing (20 W, 100 mTorr, 5 min, room temperature) and the further consolidation of the inorganic matrix and the removal of carbon impurities by O_2 RTP treatment at 600°C for 5 min (Modular Process Technology, RTP-600S).

Electrode deposition

We coated the sample with a bilayer resist consisting of 950 K PMMA A11 and 950 K PMMA A2. The resist was baked on a hot plate at 180°C for 3 min after each layer. The resist was patterned using a conventional e-beam deposition tool. Metal contacts, consisting of 10 nm of Ti and 120 nm of Au, were deposited using a ultrahigh vacuum (UHV) e-beam deposition tool following a 30-s Ar ion milling etch.

Electron microscopy

Electron microscopy was performed on Hitachi 4800 and Jeol 7600 with EDS spectrometer. EDS Spectra were collected at a minimum of 5 KeV for at least 100 k counts.

Electrical characterization

Electrical characterization was performed on a Signatone CM-170 with Agilent Analyzer. *I-V* curves were generated with medium integration time over 400 points with a step size of 100-mV steps.

For the transient photodetection study, a UV light of 340 nm was periodically switched on/off for 5 s, while the device current was logged every 50 ms steps for 150 s in total. The UV light power measured over a 1-cm–diameter area was 17 mW/cm^2.

Scanning hard x-ray microscopy

The experiment was conducted at the Hard X-ray nanoprobe (HXN 3-ID) beamline of National Synchrotron Light Source II, Brookhaven National Laboratory. Selective area–grown superlattices were coated with platinum to enhance contrast in hard x-ray imaging. Samples were prepared with an in situ lift-out procedure using Ga ion milling to fashion approximately ~1-um domain on a tungsten pin.

A monochromatic beam at 12 KeV was selected and focused by multilayer Laue lenses to a nanobeam at approximately 13 nm. Fly-scans were carried out in a grid of 150 × 120 with a step size of 20 nm by 15 nm with a 30-ms dwell time. In total, 75 projections were used for reconstruction, representing angles from −90° to +90°. Far-field diffraction was collected downstream while fluorescence was collected from an energy dispersive detector placed 90° from the beam to collect x-rays. Elements were fitted by PyXRF software package, and platinum L-edge was used to align the sample. Separately ptychography was performed on the far-field diffraction to recover the complex value probe and object function. This was used for reconstruction of the 3D volume that was performed with Tomviz (*44*) (www.tomviz.org) denoised with NAFNET (*45*) (https://github.com/megvii-research/NAFNet); further post processing and analysis were performed with Dragonfly 2023.1 ORS software Comet Technologies Canada Inc., Montreal, Canada; software is available at https://theobjects.com/dragonfly.

Supplementary Materials

This PDF file includes:

Table S1
Figs. S1 to S23

REFERENCES AND NOTES

1. B. W. Blankenship, Z. Jones, N. Zhao, H. Singh, A. Sarkar, R. Li, E. Suh, A. Chen, C. P. Grigoropoulos, A. Ajoy, Complex three-dimensional microscale structures for quantum sensing applications. *Nano Lett.* **23**, 9272–9279 (2023).
2. J. Hu, D. Mengu, D. C. Tzarouchis, B. Edwards, N. Engheta, A. Ozcan, Diffractive optical computing in free space. *Nat. Commun.* **15**, 1525 (2024).
3. P. Lin, C. Li, Z. Wang, Y. Li, H. Jiang, W. Song, M. Rao, Y. Zhuo, N. K. Upadhyay, M. Barnell, Q. Wu, J. J. Yang, Q. Xia, Three-dimensional memristor circuits as complex neural networks. *Nat. Electron.* **3**, 225–232 (2020).
4. T. Tanaka, A. Ishikawa, Towards three-dimensional optical metamaterials. *Nano Converg.* **4**, 34 (2017).
5. Z. Li, Q. Fan, Y. Yin, Colloidal self-assembly approaches to smart nanostructured materials. *Chem. Rev.* **122**, 4976–5067 (2022).
6. D. Samanta, W. Zhou, S. B. Ebrahimi, S. H. Petrosko, C. A. Mirkin, Programmable matter: The nanoparticle atom and DNA bond. *Adv. Mater.* **34**, 2107875 (2022).
7. J. S. Kahn, O. Gang, Designer nanomaterials through programmable assembly. *Angew. Chem. Int. Ed. Engl.* **61**, e202105678 (2022).
8. R. Mao, B. Minevich, D. McKeen, Q. Chen, F. Lu, O. Gang, J. Mittal, Regulating phase behavior of nanoparticle assemblies through engineering of DNA-mediated isotropic interactions. *Proc. Natl. Acad. Sci. U.S.A.* **120**, e2302037120 (2023).
9. J. S. Kahn, Y. Xiong, J. Huang, O. Gang, Cascaded enzyme reactions over a three-dimensional, wireframe DNA origami scaffold. *J. Am. Chem. Soc.* **2**, 357–366 (2022).

10. P. Wang, S. Gaitanaros, S. Lee, M. Bathe, W. M. Shih, Y. Ke, Programming self-assembly of DNA origami honeycomb two-dimensional lattices and plasmonic metamaterials. *J. Am. Chem. Soc.* **138**, 7733–7740 (2016).
11. C. Y. Zheng, W. Hadibrata, S. Kim, G. C. Schatz, K. Aydin, C. A. Mirkin, Large-area, highly crystalline DNA-assembled metasurfaces exhibiting widely tunable epsilon-near-zero behavior. *ACS Nano* **15**, 18289–18296 (2021).
12. Y. Tian, J. R. Lhermitte, L. Bai, T. Vo, H. L. Xin, H. Li, R. Li, M. Fukuto, K. G. Yager, J. S. Kahn, Y. Xiong, B. Minevich, S. K. Kumar, O. Gang, Ordered three-dimensional nanomaterials using DNA-prescribed and valence-controlled material voxels. *Nat. Mater.* **19**, 789–796 (2020).
13. J. M. Majikes, J. A. Liddle, Synthesizing the biochemical and semiconductor worlds: The future of nucleic acid nanotechnology. *Nanoscale* **14**, 15586–15595 (2022).
14. T. Hueckel, D. J. Lewis, A. Mertiri, D. J. D. Carter, R. J. Macfarlane, Controlling colloidal crystal nucleation and growth with photolithographically defined templates. *ACS Nano* **17**, 22121–22128 (2023).
15. A. M. Wong, K. Je, C. Y. Zheng, L. Jibril, Z. Miao, S. C. Glotzer, C. A. Mirkin, Arrays of colloidal single crystals engineered with DNA in lithographically defined microwells. *Nano Lett.* **23**, 116–123 (2022).
16. M. T. Hwang, M. Heiranian, Y. Kim, S. You, J. Leem, A. Taqieddin, V. Faramarzi, Y. Jing, I. Park, A. M. van der Zande, S. Nam, N. R. Aluru, R. Bashir, Ultrasensitive detection of nucleic acids using deformed graphene channel field effect biosensors. *Nat. Commun.* **11**, 1543 (2020).
17. C.-A. Vu, W.-Y. Chen, Field-effect transistor biosensors for biomedical applications: Recent advances and future prospects. *Sensors* **19**, 4214 (2019).
18. C. R. Laramy, M. N. O'Brien, C. A. Mirkin, Crystal engineering with DNA. *Nat. Rev. Mater.* **4**, 201–224 (2019).
19. J. S. Kahn, B. Minevich, O. Gang, Three-dimensional DNA-programmable nanoparticle superlattices. *Curr. Opin. Biotechnol.* **63**, 142–150 (2020).
20. A. Michelson, A. Subramanian, K. Kisslinger, N. Tiwale, S. Xiang, E. Shen, J. S. Kahn, D. Nykypanchuk, H. Yan, C.-Y. Nam, Three-dimensional nanoscale metal, metal oxide, and semiconductor frameworks through DNA-programmable assembly and templating. *Sci. Adv.* **10**, eadl0604 (2024).
21. L. Hui, R. Bai, H. Liu, DNA-based nanofabrication for nanoelectronics. *Adv. Funct. Mater.* **32**, 2112331 (2022).
22. L. Shani, A. N. Michelson, B. Minevich, Y. Fleger, M. Stern, A. Shaulov, Y. Yeshurun, O. Gang, DNA-assembled superconducting 3D nanoscale architectures. *Nat. Commun.* **11**, 5697 (2020).
23. L. Shani, P. Tinnefeld, Y. Fleger, A. Sharoni, B. Y. Shapiro, A. Shaulov, O. Gang, Y. Yeshurun, DNA origami based superconducting nanowires. *AIP Adv.* **11**, 015130 (2021).
24. X. Liu, F. Zhang, X. Jing, M. Pan, P. Liu, W. Li, B. Zhu, J. Li, H. Chen, L. Wang, Complex silica composite nanomaterials templated with DNA origami. *Nature* **559**, 593–598 (2018).
25. P. W. Majewski, A. Michelson, M. A. L. Cordeiro, C. Tian, C. Ma, K. Kisslinger, Y. Tian, W. Liu, E. A. Stach, K. G. Yager, O. Gang, Resilient three-dimensional ordered architectures assembled from nanoparticles by DNA. *Sci. Adv.* **7**, eabf0617 (2021).
26. A. Michelson, T. J. Flanagan, S.-W. Lee, O. Gang, High-strength, lightweight nano-architected silica. *Cell Rep. Phys. Sci.* **4**, 101475 (2023).
27. A. Michelson, H. Zhang, S. Xiang, O. Gang, Engineered silicon carbide three-dimensional frameworks through DNA-prescribed assembly. *Nano lett.* **21**, 1863–1870 (2021).
28. S. Wu, M. Zhang, J. Song, S. Weber, X. Liu, C. Fan, Y. Wu, Fine customization of calcium phosphate nanostructures with site-specific modification by DNA templated mineralization. *ACS Nano* **15**, 1555–1565 (2020).
29. Y. Zhao, C. Zhang, L. Yang, X. Xu, R. Xu, Q. Ma, Q. Tang, Y. Yang, D. Han, Programmable and site-specific patterning on DNA origami templates with heterogeneous condensation of silver and silica. *Small* **17**, 2103877 (2021).
30. A. Michelson, B. Minevich, H. Emamy, X. Huang, Y. S. Chu, H. Yan, O. Gang, Three-dimensional visualization of nanoparticle lattices and multimaterial frameworks. *Science* **376**, 203–207 (2022).
31. D. Adams, T. Mayer, B. Swartzentruber, Selective area growth of metal nanostructures. *Appl. Phys. Lett.* **68**, 2210–2212 (1996).
32. J. S. Lee, S. Choi, M. Pendharkar, D. J. Pennachio, B. Markman, M. Seas, S. Koelling, M. A. Verheijen, L. Casparis, K. D. Petersson, I. Petkovic, V. Schaller, M. J. W. Rodwell, C. M. Marcus, P. Krogstrup, L. P. Kouwenhoven, E. P. A. M. Bakkers, C. J. Palmstrøm, Selective-area chemical beam epitaxy of in-plane InAs one-dimensional channels grown on InP(001), InP(111) B, and InP(011) surfaces. *Phys. Rev. Mater.* **3**, 084606 (2019).
33. J. Jung, S. G. Schellingerhout, M. F. Ritter, S. C. ten Kate, O. A. van der Molen, S. de Loijer, M. A. Verheijen, H. Riel, F. Nichele, E. P. Bakkers, Selective area growth of PbTe nanowire networks on InP. *Adv. Funct. Mater.* **32**, 2208974 (2022).
34. D. J. Lewis, L. Z. Zornberg, D. J. D. Carter, R. J. Macfarlane, Single-crystal Winterbottom constructions of nanoparticle superlattices. *Nat. Mater.* **19**, 719–724 (2020).
35. C. Y. Zheng, Y. Yao, J. Deng, S. Seifert, A. M. Wong, B. Lee, C. A. Mirkin, Confined growth of DNA-assembled superlattice films. *ACS Nano* **16**, 4813–4822 (2022).
36. I. V. Martynenko, V. Ruider, M. Dass, T. Liedl, P. C. Nickels, DNA origami meets bottom-up nanopatterning. *ACS Nano* **15**, 10769–10774 (2021).
37. I. V. Martynenko, E. Erber, V. Ruider, M. Dass, G. Posnjak, X. Yin, P. Altpeter, T. Liedl, Site-directed placement of three-dimensional DNA origami. *Nat. Nanotechnol.* **18**, 1456–1462 (2023).
38. S. Adhikari, B. Minevich, D. Redeker, A. N. Michelson, H. Emamy, E. Shen, O. Gang, S. K. Kumar, Controlling the self-assembly of DNA origami octahedra via manipulation of inter-vertex interactions. *J. Am. Chem. Soc.* **145**, 19578–19587 (2023).
39. J. S. Kahn, B. Minevich, A. Michelson, H. Emamy, K. Kisslinger, S. Xiang, S. K. Kumar, O. Gang, Encoding hierarchical 3D architecture through inverse design of programmable bonds. chemRxiv [Preprint] (2022). https://doi.org/10.26434/chemrxiv-2022-xwbst
40. J. Aizenberg, A. J. Black, G. M. Whitesides, Control of crystal nucleation by patterned self-assembled monolayers. *Nature* **398**, 495–498 (1999).
41. A.-L. Barabási, H. E. Stanley, *Fractal Concepts in Surface Growth* (Cambridge Univ. Press, 1995).
42. A. Kirillov, E. Mintun, N. Ravi, H. Mao, C. Rolland, L. Gustafson, T. Xiao, S. Whitehead, A. C. Berg, W.-Y. Lo, P. Dollár, R. Girshick, Segment anything. arXiv:2304.02643 [cs.CV] (2023).
43. X. Zhao, W. Ding, Y. An, Y. Du, T. Yu, M. Li, M. Tang, J. Wang, Fast segment anything. arXiv:2306.12156 [cs.CV] (2023).
44. J. Schwartz, C. Harris, J. Pietryga, H. Zheng, P. Kumar, A. Visheratina, N. A. Kotov, B. Major, P. Avery, P. Ercius, U. Ayachit, B. Geveci, D. A. Muller, A. Genova, Y. Jiang, M. Hanwell, R. Hovden, Real-time 3D analysis during electron tomography using tomviz. *Nat. Commun.* **13**, 4458 (2022).
45. L. Chen, X. Chu, X. Zhang, J. Sun, Simple baselines for image restoration, in *European Conference on Computer Vision* (Springer Nature Switzerland, Cham, 2022), pp. 17–33.
46. A. Subramanian, N. Tiwale, W.-I. Lee, K. Kisslinger, M. Lu, A. Stein, J. Kim, C.-Y. Nam, Vapor-phase infiltrated organic–inorganic positive-tone hybrid photoresist for extreme UV lithography. *Adv. Mat. Interf.* **10**, 2300420 (2023).
47. A. Subramanian, N. Tiwale, C.-Y. Nam, Review of recent advances in applications of vapor-phase material infiltration based on atomic layer deposition. *JOM* **71**, 185–196 (2019).
48. P. Mainali, P. Wagle, C. McPherson, D. N. McIlroy, The impact of trap-assisted tunneling and Poole–Frenkel emission on synaptic potentiation in an α-Fe_2O_3/p-Si memristive device. *Sci* **5**, 3 (2023).
49. E. Leite, A. Nascimento, P. R. Bueno, E. Longo, J. A. Varela, The influence of sintering process and atmosphere on the non-ohmic properties of SnO_2 based varistor. *J. Mater. Sci. Mater. Electron.* **10**, 321–327 (1999).
50. C.-Y. Nam, A. Stein, Extreme carrier depletion and superlinear photoconductivity in ultrathin parallel-aligned ZnO nanowire array photodetectors fabricated by infiltration synthesis. *Adv. Opt. Mater.* **5**, 1700807 (2017).
51. R. Djamil, K. Aicha, A. Souifi, D. Fayçal, Effect of annealing time on the performance of tin oxide thin films ultraviolet photodetectors. *Thin Solid Films* **623**, 1–7 (2017).
52. H. Liu, M. Matthies, J. Russo, L. Rovigatti, R. P. Narayanan, T. Diep, D. McKeen, O. Gang, N. Stephanopoulos, F. Sciortino, H. Yan, F. Romano, P. Šulc, Inverse design of a pyrochlore lattice of DNA origami through model-driven experiments. *Science* **384**, 776–781 (2024).
53. G. Posnjak, X. Yin, P. Butler, O. Bienek, M. Dass, S. Lee, I. D. Sharp, T. Liedl, Diamond-lattice photonic crystals assembled from DNA origami. *Science* **384**, 781–785 (2024).
54. D. R. Miller, S. A. Akbar, P. A. Morris, Nanoscale metal oxide-based heterojunctions for gas sensing: A review. *Sens. Actuators B* **204**, 250–272 (2014).
55. R. S. Devan, R. A. Patil, J. H. Lin, Y. R. Ma, One-dimensional metal-oxide nanostructures: Recent developments in synthesis, characterization, and applications. *Adv. Funct. Mater.* **22**, 3326–3370 (2012).

Acknowledgments: This research used Materials Synthesis and Characterization, and Electron Microscopy Facilities of the Center for Functional Nanomaterials, as well as 3-ID Hard X-ray Nanoprobe (HXN) beamlines of the National Synchrotron Light Source II, both of which are the U.S. Department of Energy (DOE), Office of Science User Facilities at Brookhaven National Laboratory under contract no. DE-SC0012704. **Funding:** This work was supported by W. M. Keck Foundation. (V.P., O.G., K.R.D., and L.S.); US Department of Energy, Office of Basic Energy Sciences, grant DE-SC0008772; and US Department of Defense, Army Research Office, W911NF-22-2-0111 (O.G., D.C.R.). **Author contributions:** Conceptualization: A.M., L.S., D.C.R., N.T., J.S.K., V.P., and O.G. Methodology: A.M., L.S., W.-I.L., D.C.R., N.T., V.P., O.G., C.-Y.N., and J.S.K. Investigation: A.M., L.S., K.R.D., H.Y., A.P., C.-Y.N., W.-I.L., K.K., N.T., D.C.R., O.G., and V.P. Figures: A.M., L.S., O.G., V.P., and K.R.D. Supervision: V.P. and O.G. Writing—original draft: A.M., L.S., W.-I.L., O.G., and V.P. Writing—review and editing: A.M., L.S., W.-I.L., K.R.D., D.C.R., H.Y., C.-Y.N., J.S.K., V.P., and O.G. **Competing interests:** A.M., O.G., L.S., and V.P. have submitted a provisional patent to the US Patent and Trademark Office (USPTO) serial number SN: 63/642,412 with a filing date of 03 May 2024 related to this work. All other authors declare that they have no other competing interests. **Data and materials availability:** 3D volumetric data and transport data are available at Zenodo: https://zenodo.org/records/14548942. All data needed to evaluate the conclusions in the paper are present in the paper and/or the Supplementary Materials.

Submitted 7 October 2024
Accepted 25 February 2025
Published 28 March 2025
10.1126/sciadv.adt5620